PTEP

Prog. Theor. Exp. Phys. **2014**, 083H01 (17 pages)
DOI: 10.1093/ptep/ptu105

Characterization of a thermal neutron beam monitor based on gas electron multiplier technology

Gabriele Croci[1,4,*], Carlo Cazzaniga[2,†], Gerardo Claps[3,†], Marco Tardocchi[1,†], Marica Rebai[2,†], Fabrizio Murtas[3,†], Espedito Vassallo[1,†], Roberto Caniello[1,†], Enrico Perelli Cippo[1,†], Giovanni Grosso[1,†], Valentino Rigato[5,†], and Giuseppe Gorini[2,4,†]

[1]*Istituto di Fisica del Plasma "P. Caldirola", Associazione EURATOM-ENEA/CNR, Milano 20125, Italy*
[2]*Dipartimento di Fisica "G. Occhialini", Università degli Studi di Milano-Bicocca, Milano 20125, Italy*
[3]*Istituto Nazionale di Fisica Nucleare, Laboratori Nazionali di Frascati, Frascati 0044, Italy*
[4]*Istituto Nazionale di Fisica Nucleare, Sezione di Milano Bicocca, Milano 20125, Italy*
[5]*Istituto Nazionale di Fisica Nucleare, Laboratori Nazionali di Legnaro, Legnaro 35020, Italy*
*E-mail: croci@ifp.cnr.it

Received April 28, 2014; Revised June 13, 2014, Accepted June 30, 2014; Published August 9, 2014

Research into valid alternatives to ^{3}He detectors is fundamental to the affordability of new neutron spallation sources like the European Spallation Source (ESS). In the case of ESS it is also essential to develop high-rate detectors that can fully exploit the increase of neutron flux relative to present neutron sources. One of the technologies fulfilling these requirements is the gas electron multiplier (GEM), since it can combine a high rate capability (MHz/mm^2), a coverage area up to 1 m^2 and a space resolution better than 0.5 mm. Its use as a neutron detector requires conversion of neutrons into charged particles. This paper describes the realization and characterization of a thermal neutron GEM-based beam monitor equipped with a cathode containing ^{10}B for neutron conversion. This device is constituted by a triple GEM detector whose cathode is made of an aluminum sheet covered by a 1 μm thick $^{nat}B_4C$ layer. The method used to realize a long-lasting $^{nat}B_4C$ layer is described and the properties of such a layer have been determined. The detector performances (measured on the ISIS-VESUVIO beam line) in terms of beam profile reconstruction, imaging, and measurement of the thermal neutron beam energy spectrum are compatible with those obtained by standard beam monitors.

Subject Index H11, H50, H51

1. Introduction

The European Spallation Source (ESS) [1] that will be built in the next few years will give the possibility of enhancing the intensity of the thermal neutron flux for a wide range of experiments by a factor of 30 with respect to the existing facilities (for instance, ISIS (UK) [2], LANSCE (US) [3], TRIUMF (Canada) [4], SNS (US) [5], J-PARK (Japan) [6], and ANITA (Sweden) [7]).

The availability of such intense neutron fluxes suggests the development of large-area real-time beam monitors with a time resolution better than 1 ms and a sub-millimeter space resolution. Such monitors should be characterized by a very low neutron attenuation in order to characterize the thermal neutron beams without modifying their properties.

[†]These authors contributed equally to this work.

The detector type that best addresses these requirements is a gaseous one whose state of the art is represented by the micro-patterned gaseous detector (MPGD) [8]. Scintillating or solid-state detectors indeed cannot be easily realized in large areas, have a neutron attenuation that is obviously higher, and as a result are more expensive.

One of the MPGD technologies that are suited to this kind of application is the gas electron multiplier (GEM) one. GEMs [9] are essentially charged-particle detectors for tracking and triggering applications, as demonstrated by their frequent use in high-energy physics experiments like COMPASS (CERN) [8], TOTEM (CERN-LHC) [10], LHCb (CERN-LHC) [12], and their possible future employment in CMS-CERN (muon trackers [13]) and in ALICE-CERN (TPC: readout [12]). The GEM technology is based on a thin (50 μm) insulating foil copper-clad on both sides. This foil is perforated with a high-density, regular matrix of holes (around 100 per square millimeter) realized by photolithographic methods. Typically, the distance between the holes (pitch) is 140 μm and their diameter is about 70 μm; it is possible to realize GEM foils in different shapes such as squares [11], half-moons [10], cylinders [15], and spheres [16], and of large area [17,18]. Each hole acts as a proportional amplifier: an applied voltage to the copper layers makes a large electric field surge in the holes. In the presence of appropriate gases, single electrons entering any hole can trigger an electron avalanche. Electrons are eventually collected from the avalanche by thin electrodes (usually strips or pads) and guided towards the readout electronics.

Readouts based on strips intrinsically suffer from the problem of strip multiplicity at high interaction rates: if two particles interact at the same moment in the detector and four strips give a signal, there are two possible locations of the particles' interaction and it is not immediately possible to judge which the correct ones are. As a consequence the most promising readout pattern for using GEM detectors as beam monitors is the *padded* one: using pads instead of strips as collecting electrodes avoids the strip multiplicity issue at high rates, thus allowing the possibility of online (real-time) reconstruction of the particle beam profile without the need of a further reconstruction algorithm.

The most frequently used GEM detector technology is the triple GEM detector where three GEM foils are stacked between a cathode and an anode: since the electron amplification region is decoupled from the field induction region, the readout pattern can be designed according to experiment requirements. In addition, the electronics connected to the anode has a very low risk of being damaged by a spark, since the discharge is almost completely contained inside a GEM hole.

Triple GEM-based detectors give the possibility of achieving a very high rate capability (in the order of MHz/mm^2), a very high time resolution (around 5 ns [19]), a very narrow space resolution (50 μm), and have a very low discharge probability (10^{-7}) [20]. Recently it has also been proved that the neutron-induced discharge probability is around 10^{-8} [21].

All the above-described features make the triple GEM detector (with padded readout anode and equipped with a neutron converter [22–24]) a suitable candidate for a thermal neutron beam monitor for ESS.

A neutron converter is a material able to convert neutrons (usually through a nuclear reaction) into charged particles that can be easily detected by a GEM. Figure 1 compares the cross sections of neutron reactions in the best types of materials that can be used as thermal neutron converters.

So far the most commonly used converter in gaseous detectors is ^{3}He; most neutron facilities nowadays use ^{3}He gas tubes that give the possibility of covering large areas (m^2) and have an intrinsic efficiency to thermal neutrons $>80\%$.

Due to the current lack of ^{3}He [25] and to the limited rate capability of ^{3}He tubes, this material is not an option for detectors at ESS. Apart from gadolinium isotopes (which adsorb neutrons while

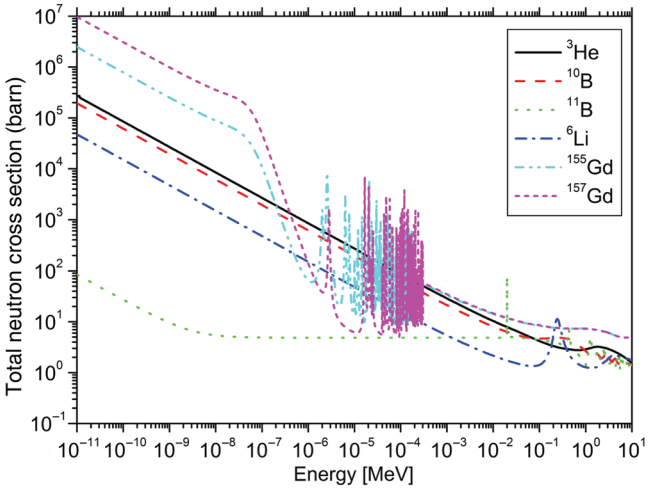

Fig. 1. Total neutron cross sections for different materials. Straight black line: ^{3}He neutron cross section as a function of neutron energy; dashed red line: ^{10}B neutron cross section as a function of neutron energy; dotted green line: ^{11}B neutron cross section as a function of neutron energy; long dashed-dotted blue line: ^{6}Li neutron cross section as a function of neutron energy; short dashed-dotted cyan line: ^{155}Gd neutron cross section as a function of neutron energy; short dashed purple line: ^{157}Gd neutron cross section as a function of neutron energy.

emitting only γ-rays as a reaction product), the one material with a thermal (i.e. with energy around 25 meV) neutron cross section similar to ^{3}He is ^{10}B. The cross section is about 3980 b and boron and thermal neutrons interact in two possible ways:

$$^{10}\mathrm{B} + \mathrm{n} \rightarrow {}^{7}\mathrm{Li} + \alpha(\text{Q-value} = 2.792\,\text{MeV}, \textit{ground state}); \text{branching ratio} = 6\%;$$
$$^{10}\mathrm{B} + \mathrm{n} \rightarrow {}^{7}\mathrm{Li}^{*} + \alpha + \gamma(0.48\,\text{MeV})(\text{Q-value} = 2.310\,\text{MeV}, \textit{excited state});$$
$$\text{branching ratio} = 94\%.$$

When thermal neutrons interact with boron, the reaction leads to ^{7}Li in the excited state 94% of the time, while the remaining 6% is ground state ^{7}Li. Conservation of energy and momentum gives $E_{\mathrm{Li}} = 0.84$ MeV and $E_{\alpha} = 1.47$ MeV for the excited state reaction, and $E_{\mathrm{Li}} = 1.16$ MeV, $E_{\alpha} = 1.78$ MeV for the ground state reaction, and implies that the two charged particles (^{7}Li and α) are emitted *back to back*. This means that at least one of the (charged) reaction products is likely to be revealed to the adjacent detector.

This paper describes the realization and test of a thermal neutron detector beam monitor prototype for ESS that is constituted by a triple GEM detector equipped with a padded anode and an aluminum cathode coated by 1 μm of $^{\mathrm{nat}}B_4C$.

2. Detector engineering

2.1. The borated cathode and its role

Figure 2(a) shows the schematics of the detector composition. The gas mixture used in this detector is Ar–CO_2 70%–30% in volume, which is the standard mix used in triple GEM detectors [10]. As can be seen, the detector is composed of a triple GEM equipped with an aluminum cathode (Al-5754, 400 μm thick) coated by 1 μm of natural boron carbide (B_4C). In order to realize a long-lasting boron deposition, the aluminum needed to undergo different manufacturing phases from smoothing

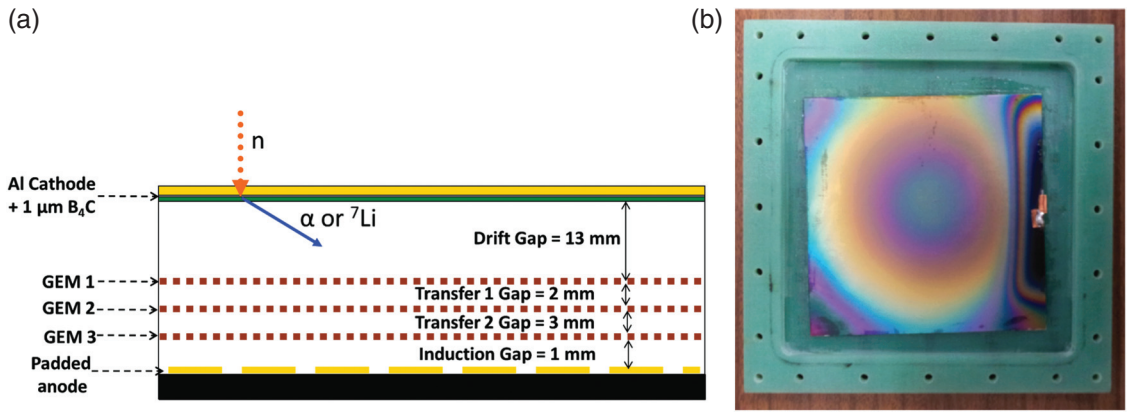

Fig. 2. (a) Detector schematics; (b) borated cathode.

to polishing. Section 2.3 describes the technique used at the Institute of Plasma Physics of the Italian National Research Council in order to realize this coating.

Figure 2(b) shows a picture of the cathode used as the thermal neutron converter: incident neutrons generate alpha particles and lithium ions (see above) emitted back to back; as a consequence only one of the two particles contributes to the signal generation. The range of alpha and lithium ions in B_4C is around 2 μm and 1 μm respectively: as a consequence these particles are able to cross the B_4C layer and reach the gas in the drift gap (the gap between the cathode and the first GEM foil), thus ionizing it. Primary electrons produced in this stage are then further multiplied by the triple GEM structure and the signal is read out by the front-end electronics connected to the padded anode. The 13 mm drift gap was chosen in order to stop all the produced charged particles (alpha and Li) in the drift gap since the range of both particles in this gas mixture is less than 10 mm. The other detector gaps (Transfer 1, Transfer 2, and Induction) were respectively 2 mm, 3 mm, and 1 mm wide. Since only one thermal neutron conversion stage is present in this detector, a detection efficiency around 1% is expected; nevertheless, since the neutron flux to be diagnosed is very high ($>10^6$ n/cm^2/s), such an efficiency is considered adequate.

2.2. *Detector readout*

Figure 3(a) shows a picture of the padded anode, which is composed of 132 8×8 mm^2 pads plus 4 L-shaped angular pads with an area of 192 mm^2. The signal of each L-shaped pad is shorted with the signal coming from 2 adjacent pads in such a way that the resulting total number of anodic signals is 128. Each signal is routed to 1 channel of one CARIOCA [26] chip whose connector is located on the back of the readout anode board. CARIOCA is an amplifier-shaper-baseline restorer-discriminator front-end chip fabricated in IBM 0.25 μm CMOS technology. Typical specification values of this chip are peaking time <15 ns for a detector capacitance less than 220 pF, equivalent noise charge $<2000 + 40$ e$^-$/pF, input resistance <50 Ohm, unipolar signal shaping, and fast baseline recovery for signals exceeding the linear range. Each chip has 8 channels with a sensitivity of 2–3 fC. The outputs of each chip are time-over-threshold low-voltage discriminated signals (LVDS). The chip is radiation tolerant and a front-end board with two of these non-encapsulated Carioca chips (the Carioca card, Fig. 3(b)) was designed at the Frascati LNF laboratories and is already being used in the LHCb experiment at CERN [12]. This card is extremely modular and usable for different GEM applications with a total dimension of 3×6 cm^2 and a channel density of 1 ch/cm^2.

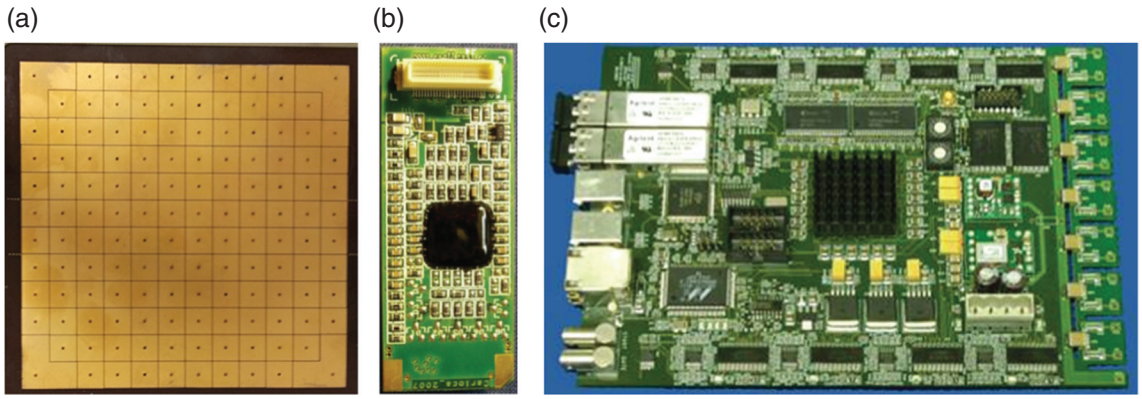

Fig. 3. Pictures of (a) the padded readout anode; (b) the CARIOCA card; (c) the FPGA motherboard.

The choice to structure the readout anode with this type of pad was taken in order to cover the maximum active area by using this electronics, which is 128-channel modular. The LVDS of each pad are managed by an FPGA motherboard (Fig. 3(c) [27], which is located on the back of the detector and which elaborates the signals in real time, thus giving the possibility of on-line monitoring of the thermal neutron beam.

2.3. B_4C deposition on aluminum cathode

2.3.1. Experimental details. Boron carbide (B_4C) and Ti coatings were sputter-deposited by an RF plasma magnetron system [28] on aluminum substrates. The apparatus consists of a parallel-plate, capacitive-coupled system, composed of a cylindrical stainless steel vacuum chamber with an asymmetric electrode configuration and with an adjustable inter-electrode gap. The powered electrode is connected to an RF (13.56 MHz) power supply, coupled with an automatic impedance matching unit, while the other electrode is grounded. Aluminum substrates were ultrasonically cleaned with acetone and ethanol, and placed on the grounded substrate holder kept at 7 cm distance from the RF-powered electrode. The vacuum before deposition was less than 1×10^{-4} Pa and the substrate temperature was monitored by using a k thermocouple placed in contact with the sample. High-purity Ar (99.9995%) gas was introduced into the chamber through a mass flow controller and a gate valve was used to adjust the pressure during the process. Ti coatings were sputter-deposited at a process pressure (3 Pa) that was kept constant by a turbo-molecular pump backed with a rotary mechanical pump. The RF power was fixed at 150 W. B_4C coatings were deposited with a multilayer structure that consists in growing different layers at different pressures. The RF power was fixed at 80 W. The morphological properties and physical structure of the films were investigated by scanning electron microscopy (SEM), atomic force microscopy (AFM), and X-ray diffraction (XRD). SEM measurements were performed using a ZEISS Supra System with an accelerating voltage of 15 kV. AFM measurements were made in air by a Nano-RTM AFM System (Pacific Nanotechnology, Santa Clara, CA, USA) operating in close contact mode. Silicon conical tips of 10 nm radius mounted on silicon cantilevers of 125 m length, 42 N/m force constant, and 320 KHz resonance frequency were used. Images were processed and analyzed by means of the NanoRule + TM software provided by Pacific Nanotechnology. The structural properties studied by X-ray diffraction measurements were performed with a wide-angle Siemens D-500 diffractometer (WAXD) equipped with a Siemens FK 60-10 2000 W tube. The radiation was a monochromatized Cu Kα beam with wavelength $\lambda = 0.154\,18$ nm. The operating voltage and current were 40 kV and 40 mA, respectively. The data were collected from

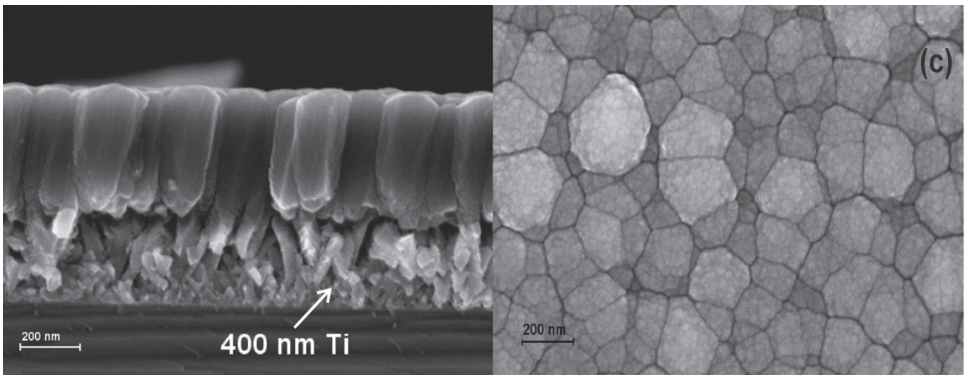

Fig. 4. SEM cross-section (left) and top-view (right) images of the B_4C coatings prepared with 400 nm of Ti interlayer thickness.

10 to 80 $2\theta^\circ$ at 0.02 $2\theta^\circ$ intervals by means of a silicon multi-cathode detector, Vortex-EX (SII). Scratch test measurements were made in compliance with the European standard UNI EN 1071-3-2005 by using a CETR UMT-2 tester equipped with a Rockwell C standard spherical diamond indenter of 50 μm radius and a 400× optical microscope.

2.3.2. Results. B_4C coatings produced by different technologies such as plasma-enhanced chemical vapor deposition [29], hot-filament chemical vapor deposition [30], and ion-beam-assisted evaporation [31] often show internal stress induced from the deposition conditions. The stress problem limits the achievable thickness of the coatings and creates difficulties for their technical applications. In order to reduce the stress of the deposited coatings, many suitable deposition recipes have been studied and optimized in terms of deposition parameters. In this study, we have produced B_4C coatings without internal stress using a titanium interlayer between the coating and the Al substrate. The Ti interlayer decreases the large discrepancy between the morphology of the substrate surface and the structure of the growing coating. In the tests performed, we found that the Ti optimal thickness was in the range 300–400 nm. Figure 4 shows SEM cross-section and top-view micrographs of the B_4C coating grown with a 400 nm Ti interlayer. The cross-sectional view allows the determination of the coating thickness, which is about 0.5 μm (obtained by a sequential deposition of four layers), implying a deposition rate of about 1.7 nm/min. The coating shows a continuous columnar structure (Fig. 4, left). The surface morphology (Fig. 4, right) is relatively uniform with grain size in the range 100–200 nm. The coating displays a smooth surface in which the root mean square roughness (R_{rms}) value, measured with a fixed area of 2 μm × 2 μm, was 15.5 nm. X-ray diffraction was used to characterize the structure. The diffraction spectrum (not shown here) reveals an amorphous feature of the coating.

In order to investigate the thermal effect during film deposition, a heated sample holder equipped with resistive heating was used. The sample holder was heated in the range 300–600 K. A four-layer B_4C coating was deposited on the substrate with about 400 nm Ti interlayer thickness. Some differences (Fig. 5) were found in the structure for coatings grown above 500 K. The continuous columnar structure becomes less visible. Evidence of this can be seen in Fig. 5 (right) (marker A) at the interface with the titanium interlayer. No significant difference was found in surface morphology. The morphology was relatively uniform for both coatings. The grain size slightly increased, as did the coating thickness, and the deposition rate increased from 1.7 to 1.9 nm/min in the range 300–600 K. Therefore, we deduce that the temperature increases the surface adatom diffusion, which gives rise to

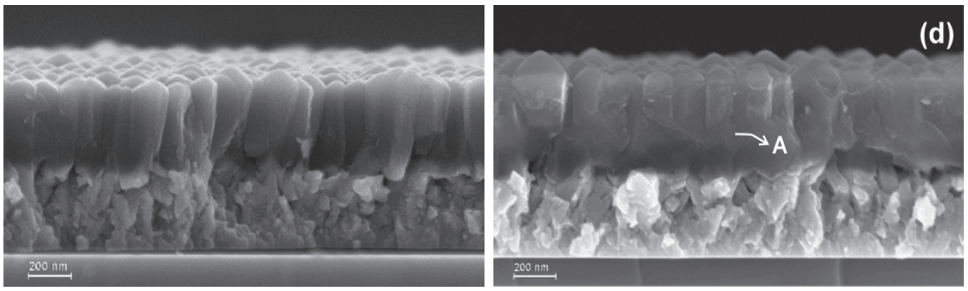

Fig. 5. SEM cross-section images of B_4C coatings prepared with a heated sample holder: (left) at 300 K and (right) at 600 K.

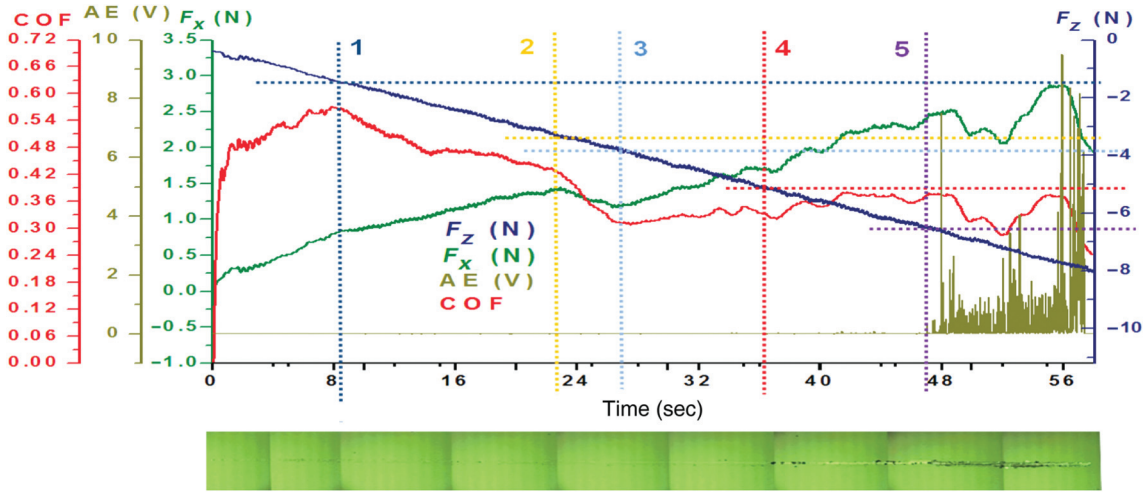

Fig. 6. Scratch test diagram. An optical micrograph of the track is shown at the bottom. Red line: coefficient of friction (COF) as a function of time; ochre line: acoustic emission (AE) as a function of time; green line: friction force (F_x) as a function of time; blue line: normal load (F_z) as a function of time.

a B_4C denser layer. The coating in this case also has an amorphous structure (diffraction not shown here).

In order to investigate the mechanical properties of the coatings, scratch test measurements were performed. In Fig. 6 the coefficient of friction (COF), the acoustic emission (AE), the indenter penetration depth (z), the friction force (F_x), and the normal load (F_z) are given as a function of time. An optical micrograph of the scratch is also shown. The scratch is performed by the progressive load scratch test (PLST) mode in which the applied normal load increases linearly with time. The slide velocity of the indenter and the applied load were fixed to 9.0 mm/min and 9.0 N/min, respectively, starting from a contact load of 0.4 N. After a short initial transient period, COF and F_x were observed to increase linearly with the load. In this region, as can be observed in Fig. 7(a), the tip interacts mainly with punctual defects of the coating. At point 1 (Fig. 6), a sharp decrease of COF and a smoother change of slope for the friction force were detected.

Looking over the optical micrograph (Fig. 7(b)), a groove within the scratch track is found, which becomes much more pronounced as the applied load increases. The coating undergoes a plastic deformation without any cracks. In the region from point 2 to point 3, a second transition in the COF and F_x was obtained. Some forward chevron cracks at the scratch track borders appear, as highlighting in Fig. 7(c). At point 4 (Fig. (6)), the first interfacial spallation of the coating can be observed

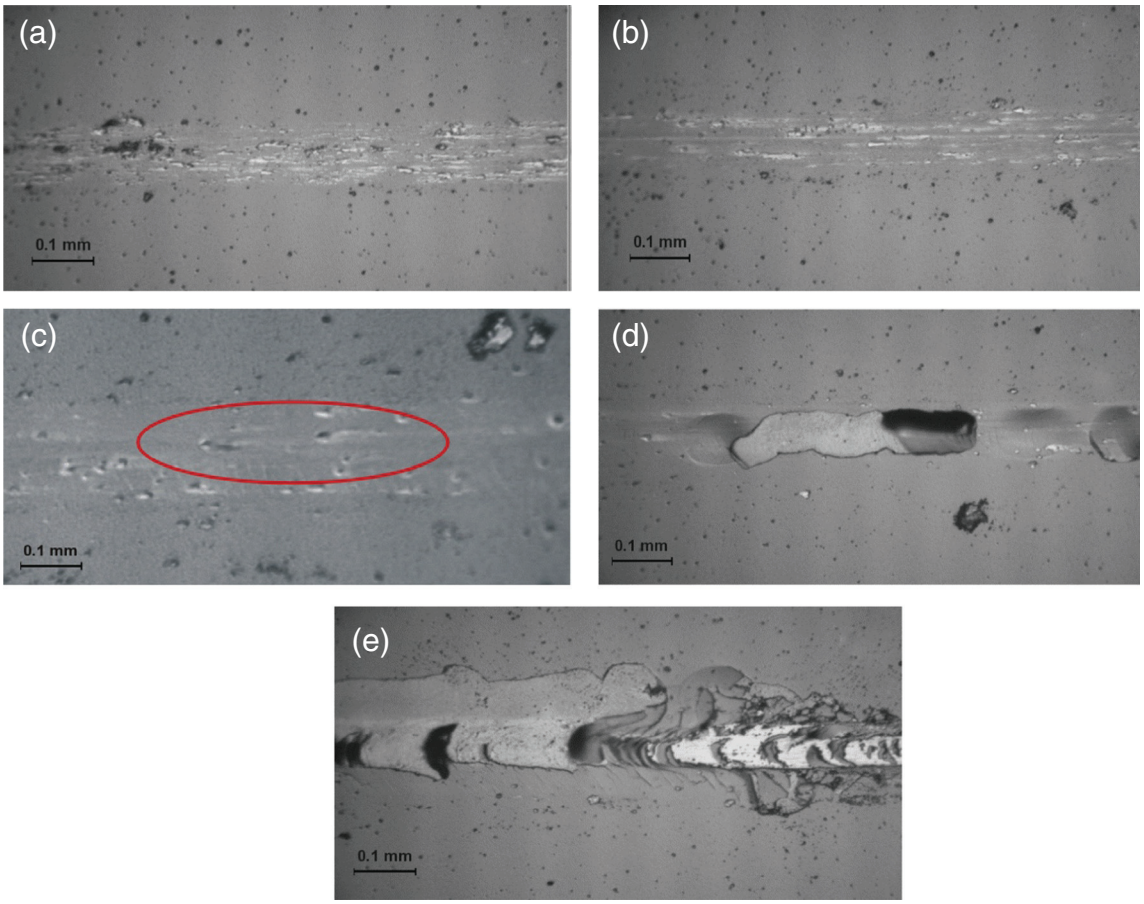

Fig. 7. 400× optical micrographs of the scratch test track. (a) Interaction tip: punctual defects of the coating; (b) plastic deformation without cracks; (c) forward chevron cracks; (d) local interfacial spallation; (e) failure of the B_4C coating and the Ti interlayer.

(Fig. 7(d)). The applied load was 5.1 N, which represents the applied critical load associated with the B_4C coating. Furthermore, tensile-type Hertzian cracks and forward chevron cracks are visible on the Ti interlayer. In the region from point 4 to point 5, the coating completely undergoes interfacial spallation. Around point 5 (Fig. 7(e)), a failure of both the B_4C and the Ti interlayer occurs at a load of 6.5 N.

A scratch test was also performed under the same conditions on a sample where no Ti interlayer was deposited. A failure of the coating occurs at a critical load of 1.4 N. A scratch test was also performed on the coating prepared with the sample holder heated to 600 K (Fig. 5, right). This coating showed a critical load (6.2 N) slightly higher than those of the room-temperature-prepared coatings. The increase in the hardness of the B_4C coatings with temperature has been reported in the literature [32]. For our B_4C coatings, however, the higher critical load of the film prepared at an elevated temperature might be related to its dense microstructure. Information concerning the film density and average stoichiometry was obtained by means of elastic back scattering (EBS) analysis. EBS analyses were carried out using a 2 MeV proton beam at a 160° back-scattering angle. The composition was obtained by simulation using the SIMNRA code [33]. As a general trend, the B/C ratio varied as a function of depth from 4 to 6, being higher towards the Ti–Ox interface. The mean B/C ratio varied for the different samples from 4.6 to 5.4. The Ti interface was partially oxidized (typical

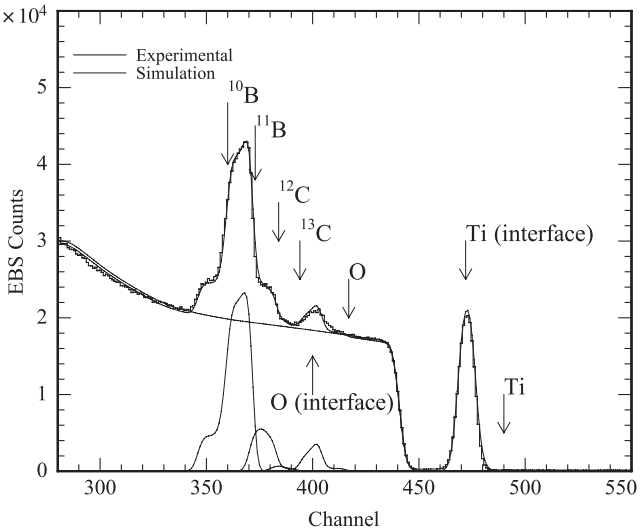

Fig. 8. Typical proton EBS spectrum of B_4C coatings deposited on a titanium adhesion layer on silicon. Simulation of different isotopes is obtained with the SIMNRA code using the most recent elastic cross section values. Thick black line: experimental data; thin black line: simulation data.

Ti/O about 0.25). The film density was calculated from the B and C elemental contents (see Fig. 8) and the SEM film thickness.

Information concerning the film density was obtained by means of Rutherford back scattering (RBS) analysis. RBS analyses were carried out using a beam of 2 MeV $^4He^+$ ions at an angle of 160° with respect to the surface of the films. The film density was calculated from the element concentration and the film thickness obtained by means of scanning electron microscopy. The films exhibited density values in the range 2.1–2.2 g/cm^3, which is close to the theoretical value of 2.5 g/cm^3 for B_4C bulk density [34].

All the realized coatings were proven to be reliable and long-lasting, thus giving the possibility of using them for a thermal neutron detector. Based on the experience developed on small-area samples, the $10 \times 10\,cm^2$ area borated cathode of the GEM detector was realized. Figure 2(b) shows a picture of the final aluminum cathode coated by 1 μm of B_4C just before being installed in the detector.

3. Detector characterization

Once the detector was completed, it was moved to a suitable neutron source (namely the VESUVIO beam line [35] at ISIS) in order to be tested in terms of capability of beam profile reconstruction and measurement of the energy spectrum of the neutron beam.

3.1. ISIS-VESUVIO facility

The measurements were performed with the detector placed in the neutron beam of the ISIS-VESUVIO [35] beam line at a distance of about 12.5 m from the neutron source. At ISIS, neutrons are produced by an 800 MeV proton beam with a double-bunch fine structure and a repetition frequency of 50 Hz. The two proton bunches are about 70 ns wide (FWHM) and 322 ns apart. The proton beam delivers an average current of 180 μA on a Ta–W target, yielding about 30 neutrons per incident proton. The VESUVIO beam line is subdued to a water moderator at ambient temperature and provides a pulsed neutron beam peaked at about 30 meV. The spectral neutron flux decreases as $1/E_n$ in the

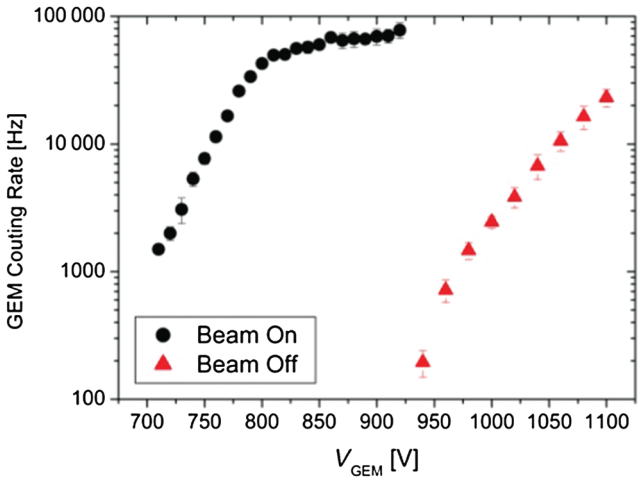

Fig. 9. Integrated GEM counting rate measurement as a function of V_{GEM} when the beam was on (neutrons and gamma rays) and off (gamma rays only). Black dots: GEM counting rate measurements with neutron beam on; red squares: GEM counting rate measurements with neutron beam off.

epithermal energy region (above 0.5 eV). At the reference position the diameter of the central area (the so-called *umbra*) of the beam-spot is about 30 mm, whereas the diameter of the *penumbra* is about 50 mm [36].

3.2. High-voltage scan and determination of working point

The gas gain of triple GEM-based detectors exponentially depends on the sum of the potential difference applied to the three GEM foils ($\Delta V_{GEM1} + \Delta V_{GEM2} + \Delta V_{GEM3} = V_{GEM}$). A suitable gain is needed in order to amplify the electronic signal generated by a charged-particle interaction with the gas medium in order to bring it above the electronic noise. Since the range of 1.5 MeV alpha particles is around 8 mm in an Ar–CO_2 70%–30% gas mixture, alphas generated by thermal neutron interaction on the borated cathode release all of their energy in the drift gap (see Fig. 2(a)), generating around 50 000 primary electrons, which correspond to a primary charge of about 8 fC. As a consequence, in order to get a signal that can be acquired using the CARIOCA chips (that must be around 1200 mV considering the chip gain), a low GEM amplification factor of 10 is sufficient ($V_{GEM} = 710$ V).

The GEM detector efficiency for different kinds of particles was measured as a function of the effective gain by varying V_{GEM} and the results are shown in Fig. 9. Two different measurements were performed: V_{GEM} scans with the neutron beam on and off, respectively. The former is a measurement of the thermal neutron detection efficiency while the latter gives a result in terms of detection efficiency for particles not time-synchronized with the beam, i.e. mainly gamma rays coming from the activation of surrounding materials. The counting rate is an increasing function of V_{GEM} and, as expected, the detector starts to detect thermal neutrons at a voltage as low as $V_{GEM} = 710$ V. A wide counting-rate plateau is present between 825 V and 925 V ($60 <$ Gain < 400): in this range the detector reaches its maximum detection efficiency while for $V_{GEM} > 925$ V the detector becomes sensitive to the gamma-ray background. The working point of the detector is determined to be 870 V; it is located at the center of the plateau and corresponds to a gain of 100: such a low gain also gives the possibility of completely rejecting the gamma-ray background that is always present during neutron

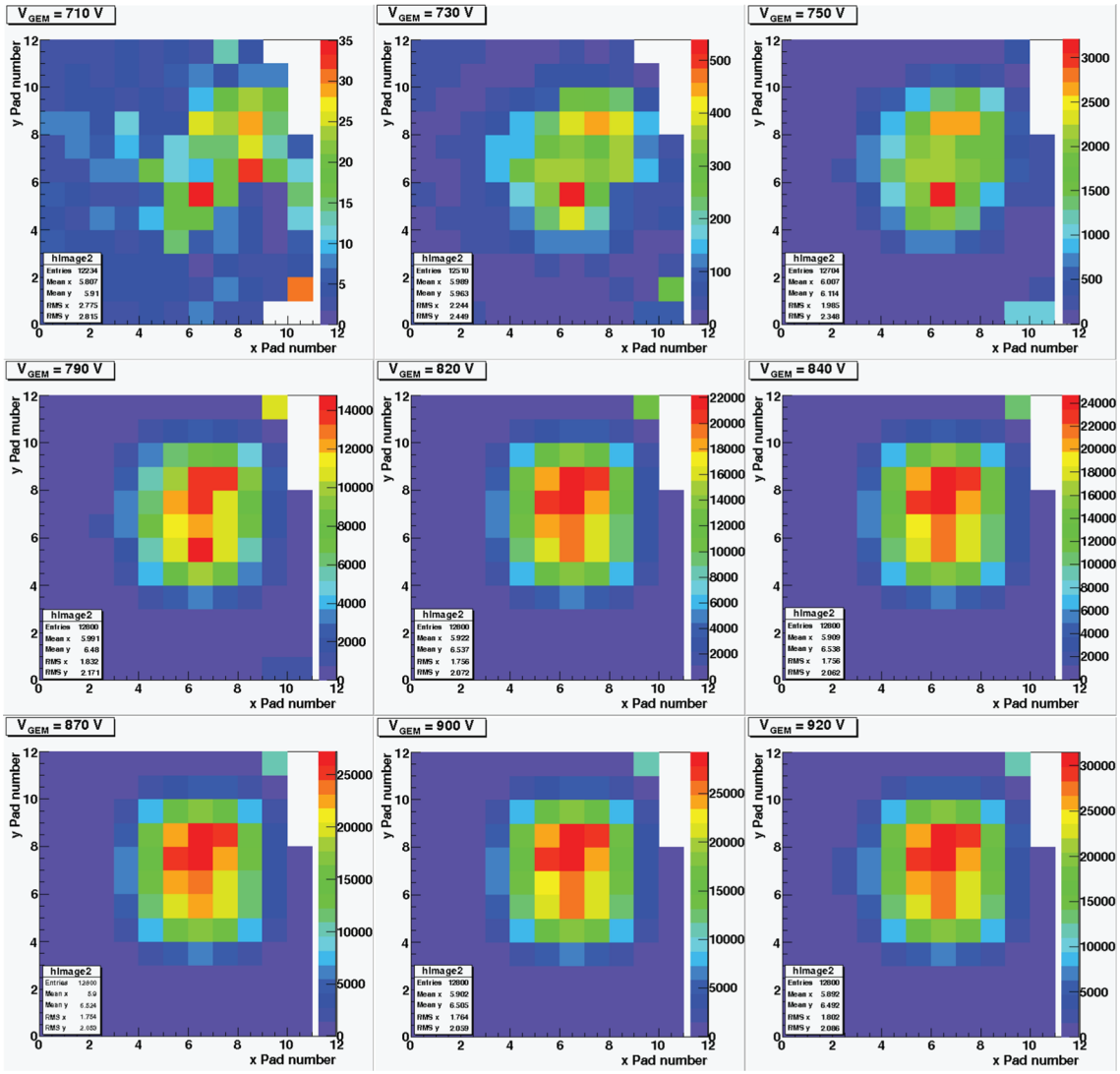

Fig. 10. Measurement of the beam profile for different V_{GEM}.

measurements. As already described in Ref. [37], the gamma-ray sensitivity for $G = 100$ is below 10^{-7} while it increases for higher gains up to 10^{-2} for $G = 10^4$.

The measured efficiency at the working point is $(7.12 \pm 0.93) * 10^{-3}$, in good agreement with the expected one for a 1 μm thick layer of natural B_4C of about $8.6 * 10^{-3}$: the two values are compatible since the measured value deviates less than two σ from the expected one. The error in the measured efficiency comes from statistical effects (the counting rate for each voltage was considered to be distributed as a Poisson function).

Figure 10 shows the measurement of the beam profile for different values of V_{GEM}: it is possible to notice that for very low gains ($V_{\mathrm{GEM}} < 790$ V; Gain < 100) the detector is not able to reconstruct the beam profile, e.g., at $V_{\mathrm{GEM}} = 710$ (Gain $= 10$), the beam profile is completely not defined. This is due to the fact that the detector efficiency is too low to be able to reconstruct all the beam components. In contrast, a well defined 2D map is observed for 800 V $< V_{\mathrm{GEM}} < 900$ V, when the detector reaches its maximum efficiency. In addition, if $V_{\mathrm{GEM}} > 900$ V, the detector also detects gamma rays and the counting rate diverges (see lateral color legends).

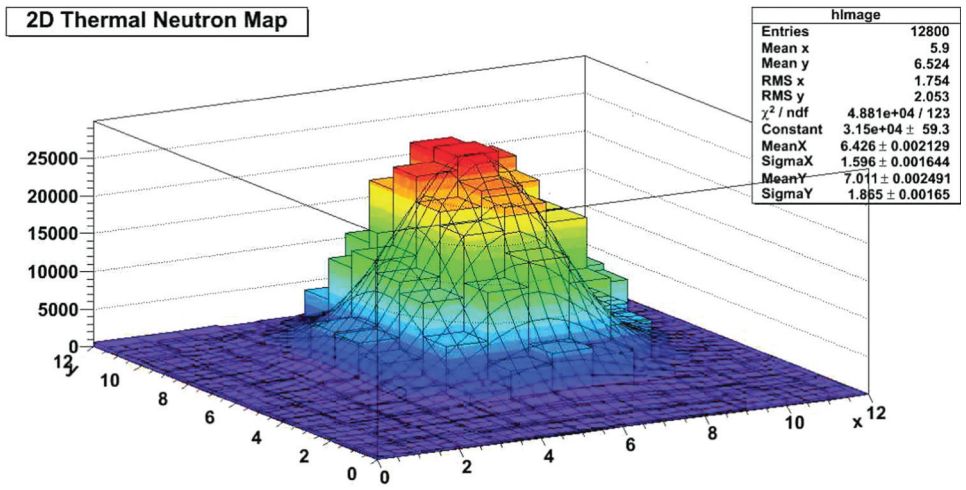

Fig. 11. Large statistics 2D map measurement and bi-Gaussian fit.

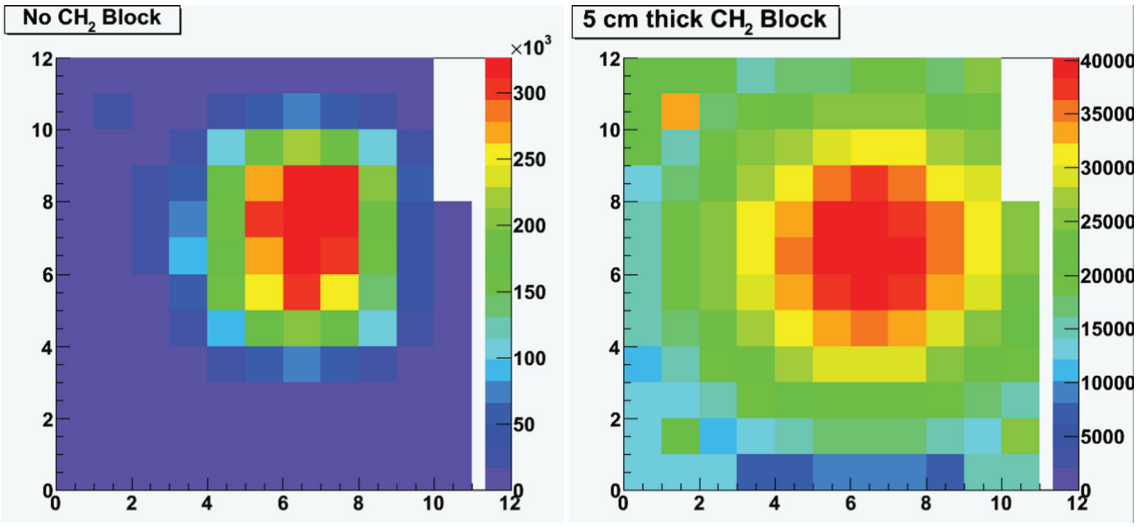

Fig. 12. Left: direct beam on the detector; right: reconstructed profile when a block of 5 cm of polyethylene is inserted in the beam in front of the detector. Z-scale (colored) shows the counts for each pad.

3.3. Measurement of the beam profile in standard conditions

Figure 11 shows a large statistics measurement of the VESUVIO beam profile at the detector working point. The reconstructed 2D map can be fitted with an X–Y bi-Gaussian function in order to determine the beam properties: an FWHMx is equal to 3.75 pads, corresponding to 3.00 cm, and an FWHMy of 4.39 pads, corresponding to 3.5 cm, were respectively measured; these values are in agreement with the expected VESUVIO beam profile widths [36].

3.4. Imaging with thermal neutrons

The imaging capability of the detector was tested by inserting some materials inside the neutron beam and comparing the obtained results to the case of a "free" beam. Two materials in particular were used: (i) a 5 cm thick polyethylene (CH_2) block positioned 1 cm away from the detector cathode and (ii) a 1 mm thick L-shaped (8 mm × 24 mm × 32 mm) cadmium sheet a few mm away from the detector cathode. The CH_2 block is a strong scatterer of thermal neutrons and, as a consequence,

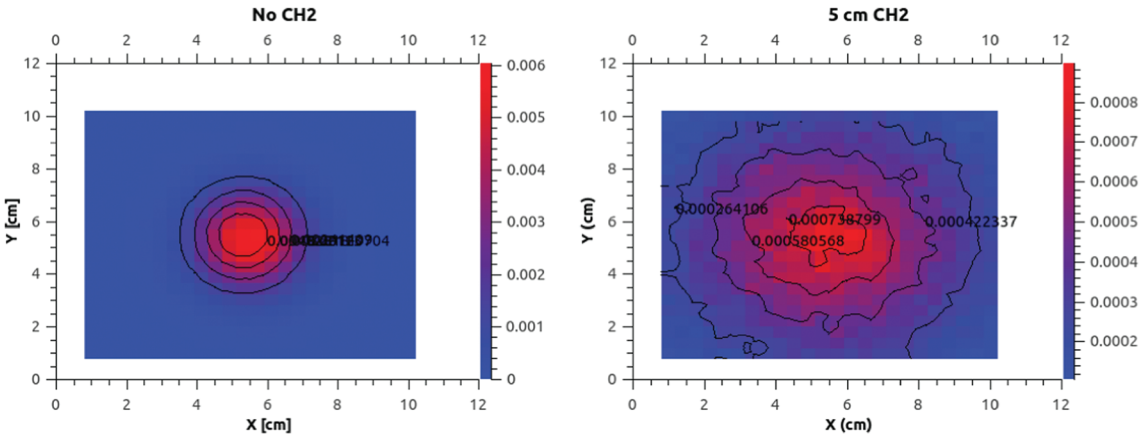

Fig. 13. MCNP simulation of the effect of the CH_2 block in front of the detector: (left) no CH_2, (right) 5 cm thick CH_2 block. Z-scale (colored) shows the counts for each position.

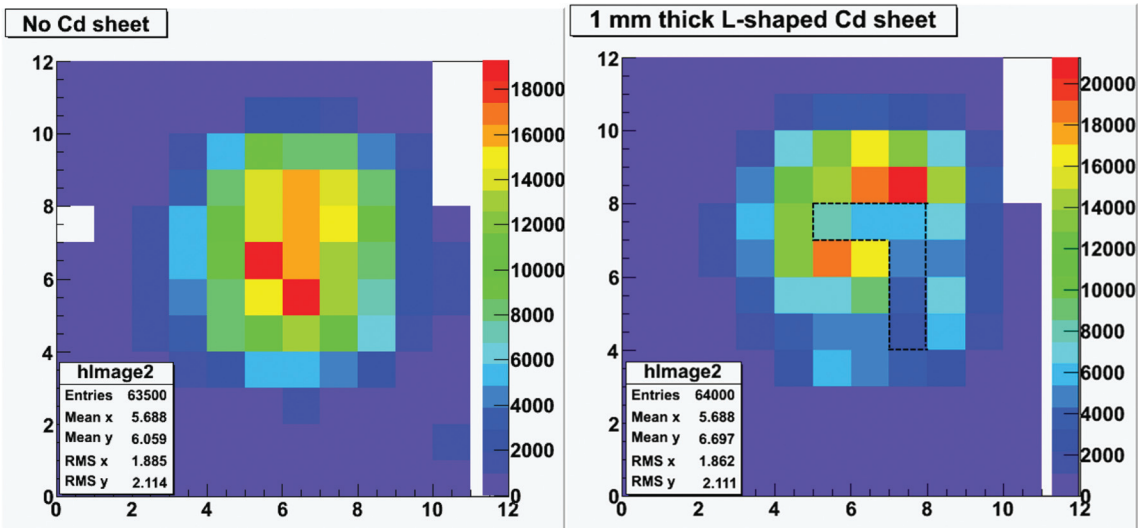

Fig. 14. Left: direct beam on the detector; right: reconstructed profile when a 1 mm L-shaped Cd sheet is positioned in front of the detector (dashed black line).

a widening of the beam is expected; on the other hand, Cd is a good absorber of thermal neutrons (since it has a total cross section higher than 1000 b for $E_n < 0.1$ eV); as a consequence, an L-shaped dip is expected in the neutron profile in correspondence to the sheet.

Figure 12 shows the measurement performed with the CH_2 block and its comparison with the free beam condition: an FWHMx equal to 11.9 pads, which corresponds to 9.5 cm, and an FWHMy of 9.9 pads, corresponding to 7.9 cm, have been measured. These measurements show that the beam profile measured on the GEM is widened by a factor of 3.1 and 2.25 for the X and Y directions respectively. In addition, the ratio between the maximum amplitude in the two cases (CH_2/no CH_2) is equal to 0.13.

Monte Carlo n-particle (MCNP) [38] calculations show that the expected beam widening is 2.38 and 1.92 respectively for the X and Y directions and that the ratio between the maximum amplitudes in the two cases (CH_2/no CH_2) is equal to 0.14 (see Fig. 13). The slight difference in the beam widening could be explained by the fact that the MCNP setup is simplified with respect to the real situation.

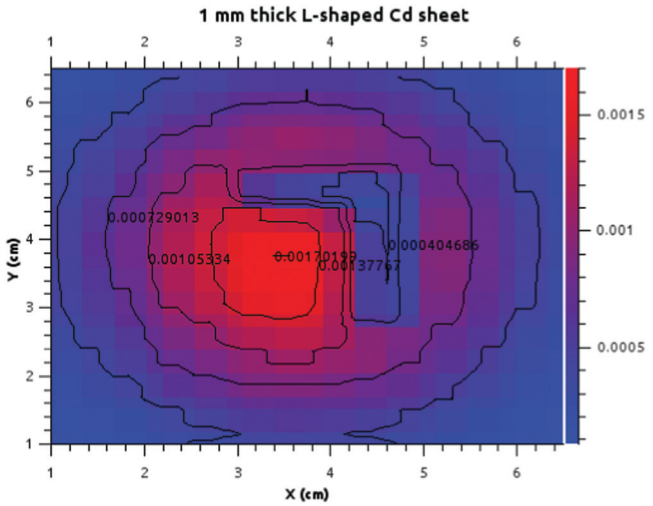

Fig. 15. MCNP simulation of the effects on the beam profile due to the L-shaped, 1 mm thick Cd sheet.

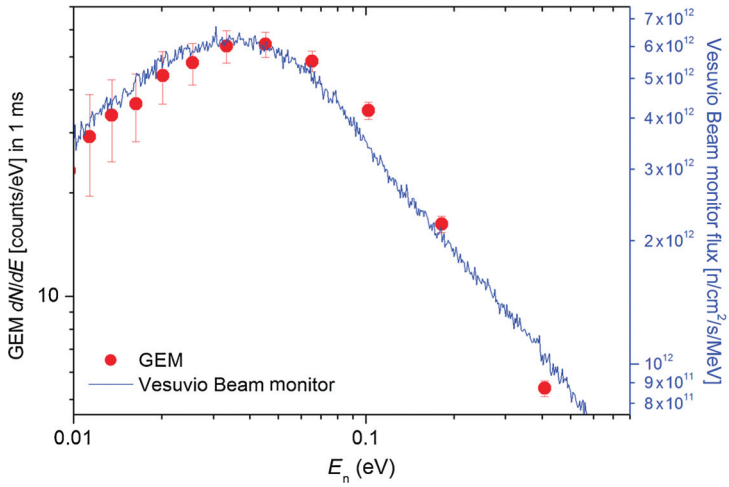

Fig. 16. GEM TOF neutron energy spectrum compared with the standard VESUVIO beam monitor spectrum. Each GEM point corresponds to the recorded counts in 1 ms and the energy difference between each point corresponds to a TOF of 1 ms. Red circles: GEM measurement; blue line: standard VESUVIO beam monitor measurement.

Figure 14 shows the measurement performed by inserting an L-shaped cadmium sheet in front of the detector. The L-shape is visible as a dip at the center of the beam profile where the total counts are reduced by a factor of 3–4 with respect to the free beam situation.

The same effect has been simulated using MCNP and the results are shown in Fig. 15. In this case, the L-shape has been reconstructed and the ratio between the dip and the free beam is between 3–4.

3.5. Measurement of the ISIS-VESUVIO beam energy spectrum using a TOF technique

The VESUVIO neutron energy spectrum was measured by using a time-of-flight (TOF) technique: the acquisition gate (1 ms wide) was delayed with respect to ISIS T_0 (the time at which the proton beam is dumped on the spallation target) in steps of 1 ms up to 15 ms. This measurement was performed in real time thanks to the multi-gate property of the MB-FPGA [27]. Figure 16 shows the result of this measurement where each point corresponds to the counts recorded in 1 ms. A comparison of GEM measurements to the spectrum measured by standard VESUVIO beam monitors

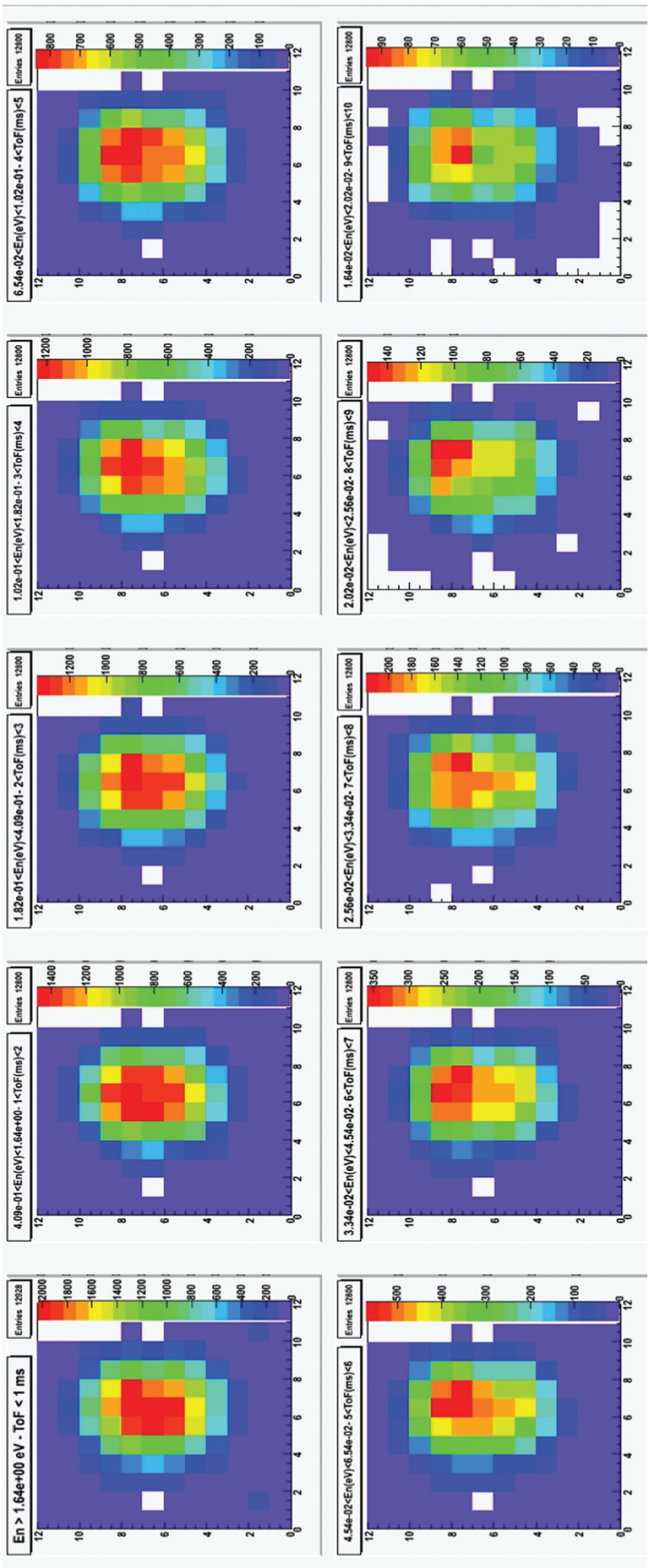

Fig. 17. 2D neutron map for different times of flight with neutron energies from 16.4 meV to 1.64 eV, corresponding to times of flight from 1 to 10 ms.

(GS20—alumina-silicate doped with ^{6}Li-oxide scintillators located in the same position as in the GEM) shows that the results obtained with the GEM and the standard monitor are fully compatible.

Figure 17 shows the evolution of the 2D map for different times of flight and as a consequence for different neutron energies, ranging from 1.64 eV to 16.4 meV (TOF from 1 to 10 ms). The beam profiles do not change significantly with neutron energy; this feature of the detector is particularly useful when it is necessary to select and monitor only neutrons that have a specific energy range, for instance for diffraction or spectroscopy measurements on defined samples.

4. Conclusions

A GEM-based thermal neutron beam monitor for ESS has been successfully realized and tested. The detector and all its components were fully realized in the framework of a collaboration between the Institute of Plasma Physics "P. Caldirola" (IFP) of the Italian National Research Council (CNR), the Italian Institute of Nuclear Physics (INFN, Laboratori Nazionali di Frascati e Sezione di Milano-Bicocca), and the physics department of University of Milano-Bicocca.

A method of realizing long-lasting and dense B_4C coatings on aluminum substrates though a plasma sputtering technique has been developed. The performance of a detector equipped with a B_4C–aluminum cathode realized through this technique has been measured at ISIS-VESUVIO, giving comparable performances to those of standard beam monitors. The capability of neutron imaging using simple samples was also tested and the results are compatible with those expected by MCNP simulations.

Other groups have developed a GEM-based thermal neutron beam monitor based on a 128×128 strip readout [39,40]. This detector (that has a double GEM structure and a ^{10}B coated aluminum cathode) is operated at a larger gas gain that the one used in the device described in this paper (500 against 100) and, due to a strip pitch of 0.8 mm, shows a better performance in terms of reconstruction of beam image (space resolution <1 mm). In addition, this detector was tested in terms of thermal neutron rate capability, showing linearity in the response up to 0.8×10^8 n/s incident on the detector. In the coming months, our detector will be exposed to a thermal neutron flux of 10^9 neutrons/$(\mathrm{cm}^2 * \mathrm{s})$ on a reactor beam in order to perform the same measurement.

The detector described in this paper represents a first step towards the realization of a high-efficiency GEM-based thermal neutron detector that can be considered an alternative to standard ^{3}He detectors. This new neutron detector will be the subject of a future publication.

Acknowledgements

We would like to thank David Dellasega (Politecnico di Milano) for supplying the SEM images and Enrico Miorin (IENI-CNR) for supplying the scratch test measurements, and A. Balla, G. Corradi, and D. Tagnani from the electronic group of Laboratori Nazionali di Frascati (INFN). This work was supported within the CNR-STFC agreement concerning collaboration in scientific research at the spallation neutron source ISIS. The financial support of *Consiglio Nazionale delle Ricerche* (CNR-Italy) is hereby acknowledged.

Funding

This work was setup in collaboration and financial support of INFN (Istituto Nazionale di Fisica Nucleare-Group5 (Technology Research) and Istituto di Fisica del Plasma "Piero Caldirola" Consiglio Nazionale delle Ricerche (EURATOM – ENEA – CNR Association).

References

[1] European Spallation Source (available at http://europeanspallationsource.se/).

[2] Science and Technology Facilities Council (UK): ISIS Facility [Available at: http://www.isis.stfc.ac.uk/index.html].
[3] Los Alamos National Laboratory (US): LANSCE Facility [Available at: http://lansce.lanl.gov].
[4] Canada's national laboratory for particle and nuclear physics: TRIUMF Facility [Available at: http://www.triumf.ca/].
[5] Oak Ridge National Laboratory SNS [Available at: http://neutrons.ornl.gov/].
[6] J-PARK: Japan Proton Accelerator Research Complex [Available at: http://j-parc.jp/index-e.html].
[7] A. V. Prokofiev et al., IEEE REDW **2009**, 166 (2009).
[8] M. Titov and L. Ropelewski, Mod. Phys. Lett. A **28**, 13 (2013).
[9] F. Sauli, Nucl. Instrum. Meth. A **386**, 531 (1997).
[10] M. G. Bagliesi et al., Nucl. Instrum. Meth A **617**, 134 (2010).
[11] G. C. Altunbas et al., Nucl. Instrum. Meth. A **490**, 177 (2002).
[12] M. Alfonsi et al., Nucl. Instrum. Meth. A **572**, 12 (2007).
[13] D. Abbaneo et al., J. Instrum. **7**, C05008 (2012).
[14] B. Ketzer, Nucl. Instrum. Meth. A, doi: 10.1016/j.nima.2013.08.027 (in press).
[15] A. Balla et al., Nucl. Instrum. Meth. A **628**, 194 (2011).
[16] S. Duarte Pinto et al., J. Instrum. **4**, P12006 (2009).
[17] M. Villa et al., Nucl. Instrum. Meth. A **628**, 182 (2011).
[18] S. Duarte Pinto et al., J. Instrum. **4**, P12009 (2009).
[19] M. Alfonsi et al., Nucl. Instrum. Meth. A **518**, 106 (2004).
[20] S. Bachmann et al., Nucl. Instrum. Meth. A **479**, 294 (2002).
[21] G. Croci et al., Nucl. Instrum. Meth. A **712**, 108 (2013).
[22] F. Murtas et al., J. Instrum. **7**, P07021 (2012).
[23] G. Croci et al., J. Instrum. **7**, C03010 (2012).
[24] G. Croci et al., Nucl. Instrum. Meth. A **720**, 144 (2013).
[25] R. T. Kouzes, Pacific North-west Laboratory, *The ^{3}He supply problem* (US Department of Energy, 2009) [Available at: http://www.pnl.gov/main/publications/external/technical_reports/PNNL-18388.pdf].
[26] W Bonivento et al., Nucl. Instrum. Meth. A **491**, 233 (2002).
[27] Design of the FPGA-MB, Gemini LNF Web Site [Available at: https://web2.infn.it/GEMINI/index.php/hvgem, date last accessed June 30, 2014].
[28] B. Despax and J. L. Flouttard, Thin Solid Films **168**, 81 (1989).
[29] A. Anne et al., Thin Solid Films **312**, 147 (1998).
[30] S. V. Deshpande et al., Appl. Phys. Lett. **65**, 1757 (1994).
[31] R. Gago et al., Thin Solid Films **373**, 277 (2000).
[32] N. Kuratani et al., Surf. Coat. Tech. **66**, 310 (1994).
[33] M. Mayer, AIP Conf. Proc. **475**, 541 (1999).
[34] J. J. Swab, S. Widjaja, and D. Singh, Advances in Ceramic Armor VII: Ceramic Engineering and Science Proceedings, Volume 32 (John Wiley & Sons, Inc., Hoboken, NJ, 2011) 81.
[35] A. N. Smirnov et al., Nucl. Instrum. Meth. A **687**, 14 (2012).
[36] S. Imberti et al., Nucl. Instrum. Meth. A **552**, 463 (2005).
[37] G. Croci et al., J. Instrum. **8**, P04006 (2013).
[38] Los Alamos National Laboratory (US), *A general Monte Carlo n-particle (MCNP) transport code* [Available at: http://mcnp.lanl.gov/].
[39] H. Oshita et al., Nucl. Instrum. Meth. A **623**, 126 (2010).
[40] H. Oshita et al., Nucl. Instrum. Meth. A **672**, 75 (2012).